This article has been accepted for publication in IEEE Transactions on Geoscience and Remote Sensing. This is the author's version which has not been fully edited and content may change prior to final publication. Citation information: DOI 10.1109/TGRS.2023.3300127

Weighted Envelope Correlation-based Waveform Inversion Using Automatic Differentiation

Chao Song, Yanghua Wang, Alan Richardson, Cai Liu

***Abstract*—Full-waveform inversion (FWI) is a popularly used high-resolution seismic inversion method. It relies on the measure of the misfit between observed data and predicted data. Due to the sinusoidal nature of seismic waves, a direct comparison of observed data and predicted data using the l_2 norm may cause cycle skipping. A variety of objective functions for FWI have been proposed to resolve this issue over the years. Based on the gradient optimization method, an explicit expression of the model gradient of the defined objective function is needed to be derived and calculated. This complicated step can be circumvented by using an automatic gradient calculation technique, called automatic differentiation (AD). AD allows calculation the gradients of the model parameters, as well as those of the inputs using the chain rule. Taking advantage of the deep-learning framework, FWI with different objective functions can be automatically optimized using AD. To improve the accuracy and applicability of FWI on real data, we propose a new objective function that we refer to as the weighted envelope-correlation inversion (WECI), which combines two correlation-based waveform inversions. The weights imposed on these two terms in this new objective function can be dynamically adjusted by the sigmoid function during the optimization process. We show the versatility and effectiveness of AD-based waveform inversions using different objective functions through numerical tests. We also demonstrate the superiority of the proposed WECI method on synthetic data and real data.**

***Index Terms*—Full-waveform inversion (FWI), cycle-skipping, envelop inversion, global correlation norm, automatic differentiation.**

I. Introduction

FULL-waveform inversion (FWI) has become an important method in seismic inversion. By taking advantage of all wave types in the seismic data, FWI can provide high-resolution estimations of subsurface parameters. The objective of conventional FWI is to minimize the misfit between the observed and predicted data [1], [2], [3]. Based on the l_2 norm constraint imposed on the data misfit, the objective function of FWI is not convex due to its high nonlinearity. When low-frequency components in the data are missing and the initial model is far away from the true model, the inversion often falls into a local minimum solution in optimizing the objective of FWI. This issue is referred to as cycle skipping.

Chao Song is with the Key Laboratory of Geophysical Exploration Equipment, Jilin University, No.938 Xi MinZhu Street, Changchun, Jilin Province 130026, China, also with the Department of Geophysics, College of Geo-Exploration Science and Technology, Jilin University, No.938 Xi MinZhu Street, Changchun, Jilin Province, 130026, China

Yanghua Wang is with Centre for Reservoir Geophysics, Imperial College London, Exhibition Road, South Kensington, London, SW7 2BP, London, UK

Alan Richardson is with Ausar Geophysical, Dalkey, Ireland

Cai Liu is with the Department of Geophysics, College of Geo-Exploration Science and Technology, Jilin University, No.938 Xi MinZhu Street, Changchun, Jilin Province 130026, China. Corresponding author: Cai Liu (E-mail: liucai@jlu.edu.cn)

A successful application of conventional FWI depends on the availability of low-frequency information in the data and a reliable background velocity model. However, in realistic seismic surveys, low-frequency components in the data are usually unavailable or contaminated by noise. Additionally, a good background velocity model is very difficult to obtain. Many methods have been proposed to invert a good background velocity model, such as traveltime tomography [4], [5], wave-equation traveltime inversion [6], [7], migration velocity analysis (MVA) [8], [9], [10], reflection waveform inversion [11], [12], etc. Though these methods can construct a good background velocity model, they impose extra challenges before the implementation of FWI.

Developing new objective functions that are immune to the cycle-skipping issue is another perspective to improve FWI. Transforming seismic data to their envelopes can produce artificial low frequencies, which will reduce the cycle-skipping issue [13], [14], [15], [16]. Wavefield reconstruction inversion (WRI) uses the wave equation as the regularization term. By controlling the weight factor imposed on the regularization term, the accuracy of the data-fitting term can be enhanced and the cycle-skipping issue can be reduced [17], [18], [19]. Adaptive waveform inversion (AWI) transforms the data fitting objective of FWI into a matching filter pursuit objective, which avoids a pixel-by-pixel data comparison [20], [21]. The Wasserstein metric-based optimal transport objective function for FWI considers the observed and predicted data as density functions and measures their global phase mismatch, which helps mitigate the cycle-skipping issue [22], [23], [24].

Besides cycle skipping, other challenges also prevent FWI from succeeding in real data applications. For example, the signal-to-noise ratio (SNR) of the raw real data is often poor. Thus, it is essential to perform data processing steps to improve the quality of the raw data. The success of conventional FWI heavily depends on the preservation of the amplitude of the data. However, the true amplitude information of the raw data can be distorted by data processing steps such as denoising. It may also be affected by receiver coupling and other acquisition issues. Thus, the development of an amplitude-independent waveform inversion is important for real data applications. [25] use logarithmic wavefields to extract the phase information and perform a phase-based waveform inversion. [26] propose to minimize the misfit of instantaneous phase extracted from the data as the objective function. [27] propose a global correlation norm (GCN) based waveform inversion to mitigate the amplitude dependency. [28] further improve the accuracy of this method by using the envelope correlation inversion (ECI).

© 2023 IEEE. Personal use is permitted, but republication/redistribution requires IEEE permission. See https://www.ieee.org/publications/rights/index.html for more information.

This article has been accepted for publication in IEEE Transactions on Geoscience and Remote Sensing. This is the author's version which has not been fully edited and content may change prior to final publication. Citation information: DOI 10.1109/TGRS.2023.3300127

These forms of waveform inversions mitigate cycle skipping in FWI to some extent. However, it takes a lot of effort and deep mathematical analysis to optimize these sophisticated objective functions. Moreover, it is difficult to merge the advantages of different waveform inversions. With the rapid development of computational resources and large amounts of available data, deep learning is increasingly attracting attention in the science and engineering fields. Deep learning has also been widely applied to improve the performance of FWI. This can be achieved from two perspectives: the data-driven perspective and the physics-informed perspective. From the data-driven perspective, deep learning can build a direct mapping between the observed data and the target velocity model through convolutional neural networks (CNNs) [14], [29], [30], [31]. This approach treats seismic inversion as an image recognition problem. Deep learning can be used to regularize FWI to improve the resolution and accuracy of the inverted models [32], [33], [34]. Researchers also apply CNNs to extrapolate low-frequency components of the data to benefit FWI and high-frequency wavefields for RTM resolution enhancement [35], [36].

Data-driven-based deep learning methods do not consider the physics laws that control the propagation of seismic waves. Their accuracy and ability to generalize highly rely on the quality and quantity of the training data, which can be difficult to assess. Physics-informed neural networks (PINNs) use physics laws as loss functions to train the networks instead of simple data mapping. PINNs have been applied to simulate seismic traveltime and wavefields [37], [38], [39], [40], [41], [42]. In PINN-based seismic inversion, separate neural networks are built to represent the velocity parameter and seismic waves. By optimizing the loss function defined by the wave equation and data fitting, the velocity model can be predicted using the trained network [43], [44], [45].

Both data-driven and physics-informed deep learning waveform inversions require enormous computational costs to complete the training of neural networks, which may even exceed the cost of a conventional FWI. Additionally, the architectures and hyperparameters of the networks need to be carefully tuned. Automatic differentiation (AD) is a crucial technique in the framework of deep learning to update the unknown parameters given in a trained network [46]. It uses the chain rule to evaluate the derivative of a function for the target parameter automatically. With the rapid development of deep learning, AD has been incorporated in the libraries of many existing deep learning computational platforms such as PyTorch [47] and TensorFlow [48], etc. Taking advantage of the feature of automatic differentiation, AD has recently been applied in FWI to form a general seismic inversion framework [49], [50], [51]. In this paper, we implement AD-based waveform inversions using different objective functions. Furthermore, we propose a new weighted ECI (WECI) method by combining two correlation-based waveform inversions, specifically GCN and ECI. We use the sigmoid function as the weight factor to balance these two terms. In the early stage of the inversion, a larger weight is imposed on ECI to recover the background velocity model. Once the low resolution components have been determined, the weight shifts to favor GCN, increasing the sensitivity of the inversion to higher resolution model components.

The rest of this paper is structured as follows. We first introduce different forms of waveform inversions and the concept of AD. Then, we demonstrate the versatility and efficacy of AD-based waveform inversions through synthetic and real data tests. We also show the superiority of the proposed method. Finally, we discuss the advantages and limitations of the proposed method and conclude our research.

II. Theory

In this section, we first compare different objective functions of waveform inversion and their corresponding gradients for the velocity model. Then, we explain the concept of automatic differentiation and its application in waveform inversion.

A. Full waveform inversion (FWI) and envelope inversion (EI)

The propagation of the seismic wave in an acoustic medium can be simulated by solving the wave equation given by:

$$m\frac{\partial^2 u(s,t)}{\partial t^2} - \nabla^2 u(s,t) = f(s,t), \tag{1}$$

where u is the pressure wavefield controlled by the model parameter m and the source function f. $m = \frac{1}{v^2}$ is defined as the squared slowness with v denoting the velocity model. s and t denote the indexes of source and time, respectively. Collecting the data from the seismic wavefield p at the locations of the receivers (r), we can get the predicted data $p(s,r,t,m)$. In conventional FWI, the l_2 norm objective function measures the misfit between the observed data and predicted data, expressed as:

$$J_{FWI}(m) = \frac{1}{2}\sum_s\sum_r\int_t \|p(s,r,t,m) - d(s,r,t)\|_2^2\, dt, \tag{2}$$

where d represents the observed data. The gradient of FWI for the model parameter can be calculated by [1]:

$$\frac{\partial J_{FWI}(m)}{\partial m} = \sum_s\sum_r\int_t \left[\frac{\partial p(s,r,t,m)}{\partial m}\cdot b_{adj}(s,r,t,m)\right] dt. \tag{3}$$

$b_{adj}^{FWI}(s,r,t,m)$ is defined as the adjoint source. In conventional least squares FWI, $b_{adj}^{FWI}(s,r,t,m) = p(s,r,t,m) - d(s,r,t)$, which is the data residual. This direct comparison of the observed and predicted data risks cycle skipping when the low-frequency components of the data are absent. To mitigate this issue, envelope inversion (EI) was proposed to retrieve the artificial low-frequency information from the data [13], [14]. The objective function of EI is expressed as:

$$J_{EI}(m) = \frac{1}{2}\sum_s\sum_r\int_t \|e_p(s,r,t,m)^q - e_d(s,r,t,m)^q\|_2^2\, dt, \tag{4}$$

where $e_p = \sqrt{p^2 + p_H^2}$ and $e_d = \sqrt{d^2 + d_H^2}$ denote the envelopes of the predicted and observed data, respectively; q is the power of envelope. d_H and p_H are the Hilbert-transformed data of d and p, respectively. The Hilbert transform of $d(t)$ is defined as:

$$H[d(t)] = \frac{1}{\pi}P\int_{-\infty}^{+\infty}\frac{d(\tau)}{t-\tau}d\tau, \tag{5}$$

© 2023 IEEE. Personal use is permitted, but republication/redistribution requires IEEE permission. See https://www.ieee.org/publications/rights/index.html for more information.

This article has been accepted for publication in IEEE Transactions on Geoscience and Remote Sensing. This is the author's version which has not been fully edited and content may change prior to final publication. Citation information: DOI 10.1109/TGRS.2023.3300127

where $H[]$ represents the Hilbert transform operation and P is the Cauchy principal value. The expressions of the model gradient of FWI (equation 2) and EI (equation 6) look similar. However, the adjoint source $b_{EI}(s,r,t,m)$ of the EI gradient is given by:

$$b_{adj}^{EI}(s,r,t,m) = A_{EI}p(s,r,t,m)e_p(s,r,m)^{q-2} - H\left[A_{EI}p_H(s,r,t,m)e_p(s,r,t,m)^{q-2}\right], \tag{6}$$

where $A_{EI} = e_p(s,r,t,m)^q - e_d(s,r,t)^q$. In the original FWI, the adjoint source b_{FWI} is simple and straightforward. By comparison, the adjoint source b_{EI} of EI is a lot more complicated and requires significant costs to implement.

B. Correlation based FWI and EI

Both FWI and EI introduced above require data fitting in terms of amplitude and phase. However, in realistic applications, the accuracy of the amplitude of the observed data may be affected by noise and other factors. In this case, direct applications of FWI and EI will not produce reliable inversion results. To mitigate the amplitude dependency, a correlation-based waveform inversion method using a global correlation norm (GCN) was proposed and proved effective in real data applications [27], [52]. The GCN-based objective function is equivalent to the zero-lag crosscorrelation between normalized observed data and predicted data, stated as [27]:

$$J_{GCN}(m) = \sum_s \sum_r \int_t \left\{-\widehat{p}(s,r,t,m)\cdot\widehat{d}(s,r,t)\right\} dt, \tag{7}$$

where $\widehat{d}(s,r,t) = \frac{d(s,r,t)}{\|d(s,r,t)\|}$ and $\widehat{p}(s,r,t,m) = \frac{p(s,r,t,m)}{\|p(s,r,t,m)\|}$ are defined as normalized observed and predicted data, respectively. The gradient of GCN-based waveform inversion is similar to equation 3. The form of the adjoint source for GCN $b_{adj}^{GCN}(s,r,t,m)$ is given by:

$$b_{adj}^{GCN}(s,r,t,m) = \frac{1}{\|p(s,r,t,m)\|}\cdot \left\{\widehat{p}(s,r,t,m)\left(\widehat{p}(s,r,t,m)\cdot\widehat{d}(s,r,t)\right) - \widehat{d}(s,r,t)\right\}. \tag{8}$$

Even though the GCN-based waveform inversion can mitigate the amplitude dependency, it still suffers from the cycle-skipping issue, which is considered the biggest challenge in FWI. Since transforming the data to its envelope can generate low-frequency components, it is natural to utilize the envelope of the data in the correlation-based waveform inversion to form an envelope correlation-based inversion (ECI), stated as [28]:

$$J_{ECI}(m) = \sum_s \sum_r \int_t \{-\widehat{e_p}(s,r,t,m)^q\cdot\widehat{e_d}(s,r,t)^q\}\, dt, \tag{9}$$

where $\widehat{e_u}(s,r,t)^q = \frac{e_p(s,r,t)^q}{\|e_p(s,r,t)^q\|}$ and $\widehat{e_d}(s,r,t)^q = \frac{e_d(s,r,t)^q}{\|e_d(s,r,t)^q\|}$. Based on the adjoint-state method, the gradient of $J_{ECI}(m)$ is similar to the gradients of other waveform inversion methods. However, the expression of the adjoint source $b_{adj}^{ECI}(s,r,t,m)$ is much more complicated, which is shown as:

$$b_{adj}^{ECI} = p\left\{A_{ECI}pe_p)^{q-2} - H\left[A_{ECI}p_H e_p^{q-2}\right]\right\} \tag{10}$$

with

$$A_{ECI} = \frac{1}{\|e_p(s,r,t,m)^q\|} \{\widehat{e_p}(s,r,t,m)^q\,(\widehat{e_p}(s,r,t,m)^q\cdot\widehat{e_d}(s,r,t)^q) - \widehat{e_d}(s,r,t)^q\}. \tag{11}$$

From equation 6 and equation 10, we observe that the main energy of the adjoint source $b_{ECI}(s,r,t,m)$ is determined by the envelopes of the data. Thus, the gradient of ECI will produce artificial low-frequency components. Though this feature will somewhat address the cycle-skipping issue, it will reduce the resolution of the inverted models. Envelope-based waveform inversion methods are usually used to generate a good starting model for a subsequent FWI application. Instead, a single method that can invert for both low and high resolutions is desirable.

C. Weighted ECI (WECI)

In the early stage of waveform inversion, low-wavenumber model updates are preferred to build a good background velocity model. Once the background model has been determined, the method can focus on higher wavenumber components to refine the resolution of the inverted models. To achieve this goal, we propose a weighted ECI objective function by combining the advantages of the aforementioned GCN and ECI methods, which can be stated as:

$$J_{WECI}(m) = w(i)J_{GCN}(m) + (1-w(i))\,J_{ECI}(m), \tag{12}$$

where $w(i)$ denotes a weight factor with i standing for the iteration number of the optimization. We use the sigmoid function to define the weight factor $w(i)$ for the iterations, which is given by:

$$w(i) = \frac{1}{1+e^{-(i-\frac{N}{2})}},\quad i = 1,...,N. \tag{13}$$

Assuming the total iteration number $N = 200$, Figure 1 shows how the weight factor changes with the iteration number. We observe that, during the optimization process, the weight factor $w(i)$ is equal to zero when the iteration number i is relatively small. It will gradually increase as the iteration number i grows. When i is relatively large, the weight factor $w(i)$ will become one. Consequently, a large weight is imposed on ECI to recover the background model at the beginning of the inversion. Then, the weight imposed on ECI gradually decreases and the impact of the ECI term weakens. In the meantime, the weight of the GCN term increases to improve the resolution of the inverted velocity model.

The gradient of WECI with respect to the model parameters can be obtained by a weighted summation of equation 9 and equation 12, which is complicated to compute. To simplify the gradient derivation and calculation, we use a deep-learning-based technique called automatic differentiation to achieve automatic derivation and calculation of the WECI gradient.

© 2023 IEEE. Personal use is permitted, but republication/redistribution requires IEEE permission. See https://www.ieee.org/publications/rights/index.html for more information.

This article has been accepted for publication in IEEE Transactions on Geoscience and Remote Sensing. This is the author's version which has not been fully edited and content may change prior to final publication. Citation information: DOI 10.1109/TGRS.2023.3300127

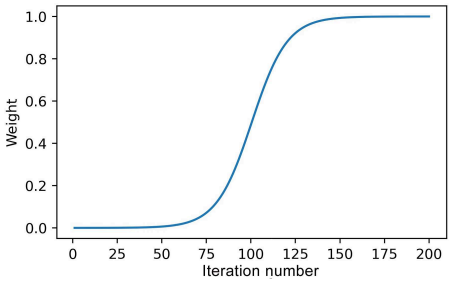

Fig. 1. Weight values for different iteration numbers.

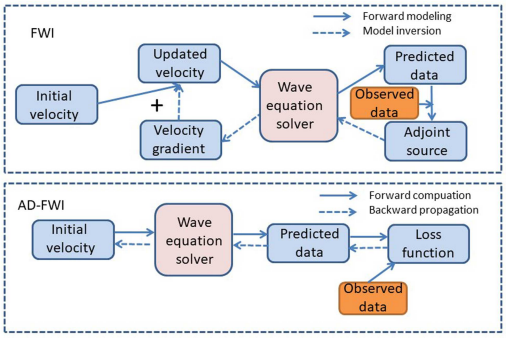

Fig. 2. (a) Workflows for waveform inversions based on the adjoint-state method and (b) the automatic differentiation (AD) method.

D. Automatic differentiation (AD)

AD is a technique that evaluates the derivative of a function through symbolic and numerical evaluations. In deep learning, AD has become an essential technique in training neural networks by backpropagating the loss. It admits an exact computation of the derivative of a function. It does not suffer from the truncation error in the numerical differentiation using the finite-difference method. Though symbolic differentiation is also exact, it causes the expression swell issue when the target function is complicated [53]. Unlike symbolic differentiation, which gives a mathematical expression of a function's derivative, AD uses the chain rule to break complex expressions into simpler ones and uses numerical evaluations in the intermediate steps, it is achieved by manipulating blocks of computer programs.

In AD-based waveform inversion, the objective function is treated as the loss function of a deep-learning task. While the velocity model is used as trainable parameters that can complete the data-fitting task. Let us compare the workflows of waveform inversion based on the adjoint-state method and the automatic differentiation method shown in Figure 2. We see that the derivation and calculation of the adjoint source is an essential step in the adjoint-state-based waveform inversion. However, this step causes difficulties for sophisticated objective functions. By comparison, AD-based waveform inversion can avoid this step and automatically compute the velocity gradient by backpropagating the defined training loss. We implement AD-based waveform inversions using a module developed in PyTorch called *Deepwave* [54]. AD-based waveform inversion is often more efficient than conventional implementations of waveform inversion as it can be accelerated by parallel computing and graphics processing units (GPUs) [55].

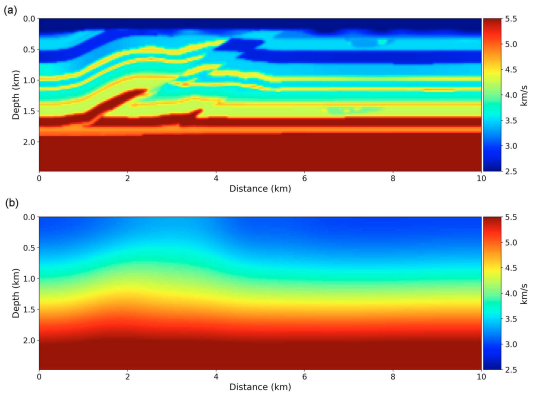

Fig. 3. (a) The true 2D Overthrust model, and (b) the highly smoothed initial velocity model.

III. Results

In this section, to show the efficacy and versatility of AD-based waveform inversion, we implement them for different objective functions on synthetic and real data. We compare the performances of different objective functions and demonstrate that the proposed WECI method can generate accurate high-resolution inversion results.

A. Overthrust model

We consider the Overthrust model as the first test [56]. The size of the model is 401×100, and the spatial sampling interval is 25 m in both vertical and horizontal directions. The true and initial velocity models are shown in Figures 3a and 3b, respectively. We obtain the initial velocity by smoothing the true velocity with a 1000 m$\times$1000 m Gaussian window. The detailed structures of the true model are smeared in the initial velocity model.

We use a 6-Hz Ricker wavelet to generate the synthetic seismic data. The frequencies below 3 Hz are filtered out. The filtered wavelet and its envelopes are shown in Figure 4a. It is obvious that the envelopes are less oscillatory than the original wavelet. When the power value q of the envelope equals 2, the envelope becomes thinner as the small values get even smaller after a square operation. Figure 4b displays the corresponding spectra of the filtered Ricker wavelet and its envelopes. We observe that low-frequency components of the wavelet are missing. However, the envelope of the wavelet produces artificial low frequencies. When we increase the power value q, the resulting envelope can recover a slightly wider range of low frequencies.

We ignite 80 sources uniformly distributed on the surface and use a recording time of 3 s. One shot gather is shown in Figure 5a. Figures 5b-5d show the data envelopes when q equals 1, 2, and 1.5, respectively. Compared to the original data, the events of the envelope data are thicker, which will help reduce the cycle skipping. However, when the power

© 2023 IEEE. Personal use is permitted, but republication/redistribution requires IEEE permission. See https://www.ieee.org/publications/rights/index.html for more information.

This article has been accepted for publication in IEEE Transactions on Geoscience and Remote Sensing. This is the author's version which has not been fully edited and content may change prior to final publication. Citation information: DOI 10.1109/TGRS.2023.3300127

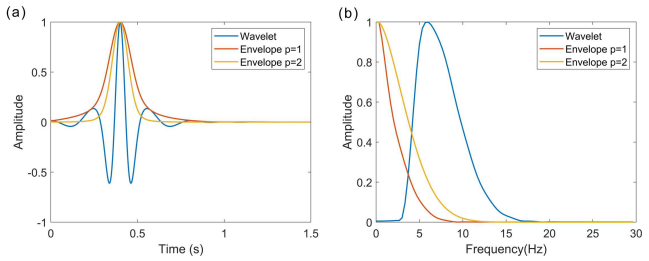

Fig. 4. (a) The filtered Ricker wavelet (blue line) and its envelope for $q = 1$ (red line) and $q = 2$ (orange line). (b) The corresponding spectra of the filtered Ricker wavelet (blue line) and its envelopes for $q = 1$ (red line) and $q = 2$ (orange line).

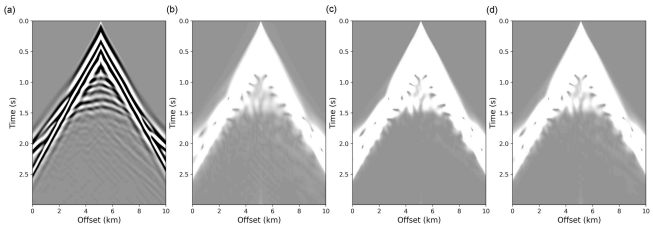

Fig. 5. (a) One shot gather from the true data, (b) data envelope ($q = 1$), (c) data envelope ($q = 2$), and (c) data envelope ($q = 1.5$).

value of the envelope is bigger, the energy of the deep reflections is weaker. This will cause poor illumination for deep structures of the subsurface.

We implement AD-based waveform inversions using a variety of objective functions introduced above, such as l_2 norm, GCN, ECI, and WECI. Figures 6a and 6b display the raw normalized velocity gradients from l_2 norm and GCN objective functions. Figures 6c-6e display the velocity gradients of ECI when q equals 1, 2, and 1.5, respectively. AD-based waveform inversion calculates the velocity gradients implicitly, so we obtain them by subtracting the initial velocity from inverted velocity models after one iteration. Figure 6f is the slightly smoothed true velocity perturbation used as an ideal reference velocity gradient. We observe that the energy of the velocity gradients in Figures 6a and 6b span the whole model domain, but some detailed structures cannot be accurately estimated, like the framed area in Figure 6f. Additionally, there exist abrupt changes in the velocity gradients produced by the l_2 norm and GCN objective functions. By comparison, the velocity gradients from ECI are a lot smoother and their main energy focuses on the shallow area. The larger q gets, the shallower ECI will cover.

After 150 iterations of velocity updates, the inverted models from l_2 norm and GCN objective functions are shown in Figures 7a and 7b, respectively. We observe that the conventional FWI and GCN-based waveform inversion fail to recover the accurate structures of the true velocity model due to the cycle-skipping problem. Figure 7c displays the ECI-inverted velocity model when $q = 1$. The accuracy of the inverted model is better thanks to the artificial low frequencies produced by the envelope, but some velocity updates on the edge of the model are incorrect (indicated by the circle). When we increase the value of q to 2, the inverted velocity (Figure 7d)

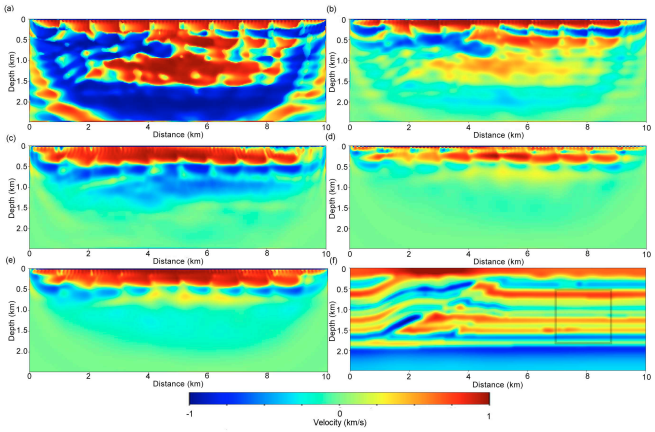

Fig. 6. The raw normalized gradients from (a) l_2 norm objective function, (b) GCN, (c) ECI ($q = 1$), (d) ECI ($q = 2$), (e) ECI ($q = 1.5$), and (f) the slightly smoothed true velocity perturbation.

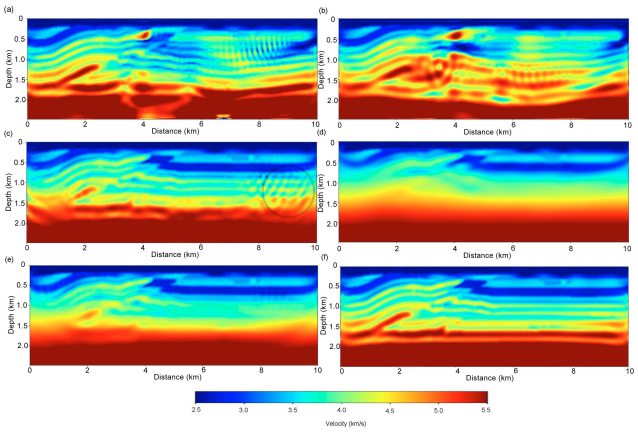

Fig. 7. The inverted velocity models from (a) l_2 norm, (b) GCN, (c) ECI ($q = 1$), (d) ECI ($q = 2$), (e) ECI ($q = 1.5$), and (f) the proposed WECI ($q = 1.5$).

is smoother, but the deep structure cannot be updated in this case. By comparison, an intermediate q value ($q = 1.5$) can not only preserve the smooth feature of velocity updates but also provide partial recovery for deep structures, as indicated by Figure 7e. However, ECI with $q = 1.5$ still requires a subsequent FWI application to refine the resolution of the inverted model.

Finally, we implement the proposed WECI using the same inversion setup. The weights $w(i)$ of WECI for this example are given by: $w(i) = \frac{1}{1+e^{-(i-\frac{N}{3})}}$ and the resulting weight values for different iterations are shown in Figure 8. As the initial velocity model for this example is generally good, we only need a limited number of big weights imposed on the ECI term to construct a good starting model. The weights of the GCN term are gradually increased to refine the resolution of the inverted velocity model as shown in Figure 7f. We observe that all the detailed structures are recovered by the proposed WECI.

© 2023 IEEE. Personal use is permitted, but republication/redistribution requires IEEE permission. See https://www.ieee.org/publications/rights/index.html for more information.

This article has been accepted for publication in IEEE Transactions on Geoscience and Remote Sensing. This is the author's version which has not been fully edited and content may change prior to final publication. Citation information: DOI 10.1109/TGRS.2023.3300127

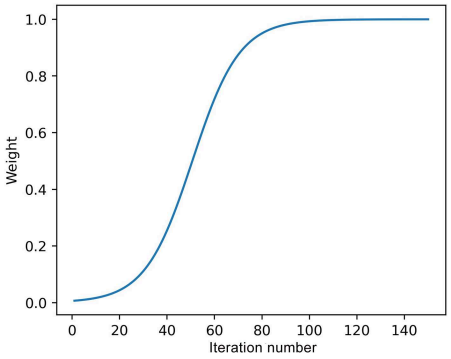

Fig. 8. Weight values in WECI for different iterations.

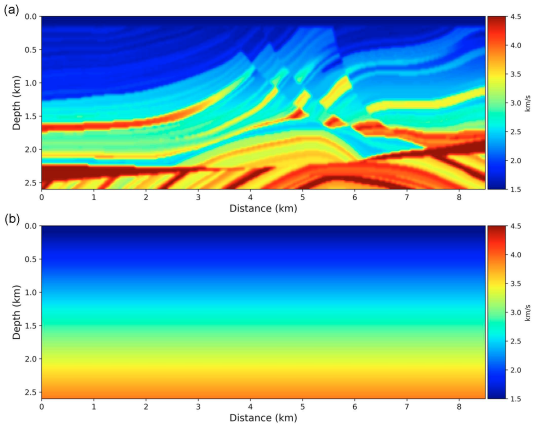

Fig. 9. (a) The true 2D Marmousi model, and (b) the initial velocity model.

B. Marmousi model

We next test the proposed WECI method on the Marmousi model [57]. The size of the model is 121×370, and the vertical and horizontal spatial sampling interval is 25 m. The true and initial Marmousi models are shown in Figures 9a and 9b, respectively. The initial velocity is linearly increasing with depth, which is far from the true model.

We use a filtered Ricker wavelet (>3 Hz) to generate 72 shot gathers as the synthetic observed seismic data. The recording time is 6 s. The sources are uniformly distributed on the surface. All the grid points on the surface act as the receivers. In this example, we perform AD-based FWI, GCN, ECI ($q = 1.5$), and WECI ($q = 1.5$) using 200 iterations. The inverted velocity models from FWI and GCN are shown in Figures 10a and 10b, respectively. As the quality of the initial model is poor and the low-frequency components of the data are absent, the inverted models suffer severely from the cycle-skipping problem, as indicated by the circle areas. The high-velocity layers identified by the black arrows in Figures 10a and 10b are mislocated.

The ECI-inverted ($q = 1.5$) velocity model is shown in Figure 10c. We observe that ECI can invert the general structures in the shallow area, but it fails to recover the detailed information of the whole model. For the proposed WECI method, the weights $w(i)$ for ECI and GCN terms of different

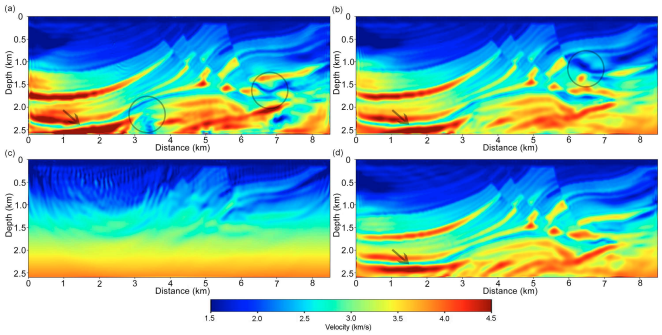

Fig. 10. The inverted velocity models from (a) FWI, (b) GCN, (c) ECI ($q = 1.5$), and (d) the proposed WECI ($q = 1.5$).

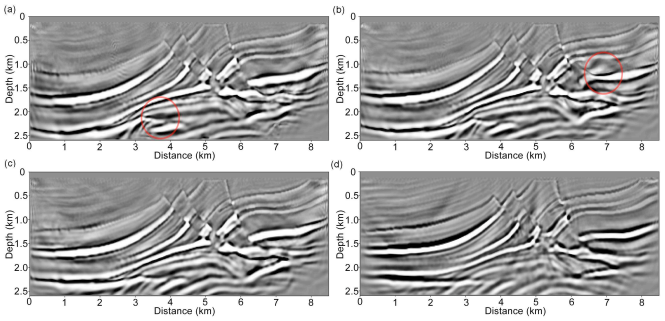

Fig. 11. The LSRTM images from (a) FWI-inverted velocity model, (b) GCN-inverted, (c) WECI-based inverted, and (d) the true velocity models.

iterations are shown in Figure 1. The initial velocity model is crude in this example. Thus, we use balanced weights for ECI and GCN to contribute. In the early stages, ECI dominates the optimization and it builds a good starting model for GCN. Gradually, GCN starts to dominate the velocity update and inject the details into the inverted model. Consequently, all the detailed structures of the true model are reconstructed by WECI, even the high-velocity layer pointed by the black arrow.

To further evaluate the accuracy of the inverted velocity models, we perform least-squares reverse time migration (LSRTM) on them and the resulting images are shown in Figure 11. We implement LSTRM using *Deepwave*. We observe that some events in the LSTRM images from FWI- and GCN-inverted velocity models are seriously distorted due to the velocity errors, as indicated by the red circles in Figures 11a and 11b. Figure 11c displays the LSTRM image obtained from the WECI-based inverted velocity model. Figure 11d displays the reference LSTRM image obtained from the true velocity model. The images show that the energy of the events in Figure 11c is well focused on the right locations (compared to Figure 11d), which indicates the accuracy of the WECI-based inverted velocity model.

Figure 12 displays the vertical velocity profiles at the distance of 5 km to show a detailed velocity comparison. The profiles show that all the inverted velocity models fit well with the true velocity in the shallow area (0-1.5 km depth). However, the velocity profiles from FWI and GCN deviate from the true velocity in the deep area. While the WECI-inverted velocity agrees with the true velocity very well.

© 2023 IEEE. Personal use is permitted, but republication/redistribution requires IEEE permission. See https://www.ieee.org/publications/rights/index.html for more information.

This article has been accepted for publication in IEEE Transactions on Geoscience and Remote Sensing. This is the author's version which has not been fully edited and content may change prior to final publication. Citation information: DOI 10.1109/TGRS.2023.3300127

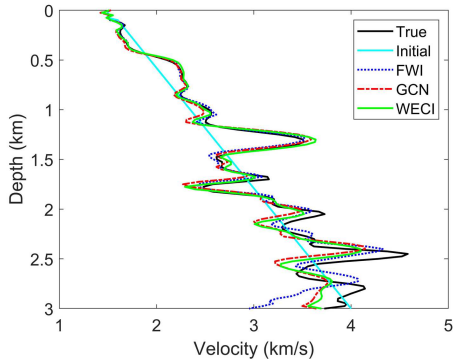

Fig. 12. The vertical velocity profile at the distance of 5 km (black solid curve: true velocity; cyan solid curve: initial velocity; blue dotted curve: FWI-inverted velocity; red dash-dotted curve: GCN-inverted velocity; green solid curve: WECI inverted velocity).

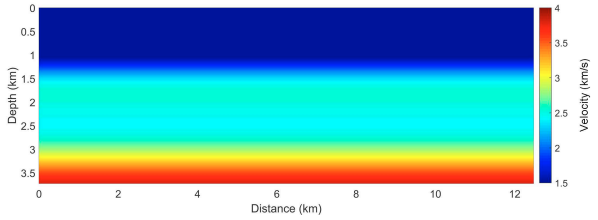

Fig. 13. The initial velocity model.

C. 2D real data

Finally, we test the proposed WECI method on 2D real data acquired by CGG from the North-Western Australia Continental Shelf [58], collected using the Broadseis acquisition system. In the original data, there are 1824 shot gathers. Due to the limitation of our computational resources, we select 100 shot gathers from them to cover our target survey area, stretching 12.5 km laterally and 3.75 km depth. For each selected shot gather, there are 324 receivers from streamer acquisition with an interval of 25 m. The initial velocity does not vary horizontally and no detailed information is provided, which is shown in Figure 13.

Low frequencies < 2.5 Hz in the raw data are contaminated by noise. Thus, they cannot be used in the inversion. We implement WECI in two stages. In the first one, we invert the velocity model using bandpass-filtered data within a frequency range from 2 Hz to 8 Hz. One filtered shot gather (2-8 Hz) from the real data is shown in Figure 14a. Setting $q = 1.5$, the data envelope is shown in Figure 14b. The source wavelets for each shot gather used in the WECI are extracted from direct waves by backpropagating them to the source locations.

Compared to the original amplitude-dependant least-squares FWI, correlation-based waveform inversions are more suitable in real data applications. We first implement GCN on the filtered real data. Then, we perform WECI using the same inversion setup. The weights used in the real data are the same as the Marmousi example (Figure 1). The raw velocity gradients of GCN and WECI (ECI is dominating) for the first iteration are shown in Figures 15a and 15b, respectively. By comparison, the raw velocity gradient from WECI shows

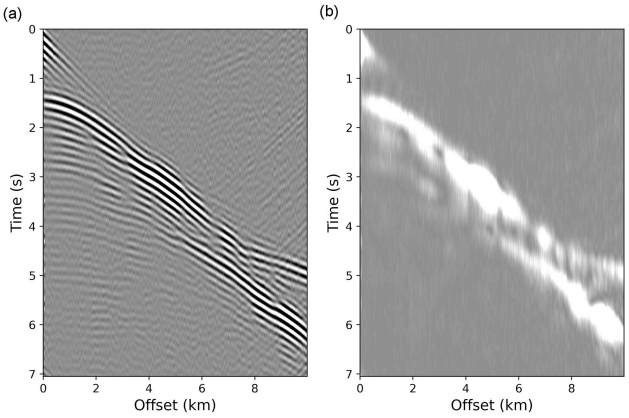

Fig. 14. (a) One filtered shot gather (2-8 Hz) from the real data, and (b) data envelope ($q = 1.5$).

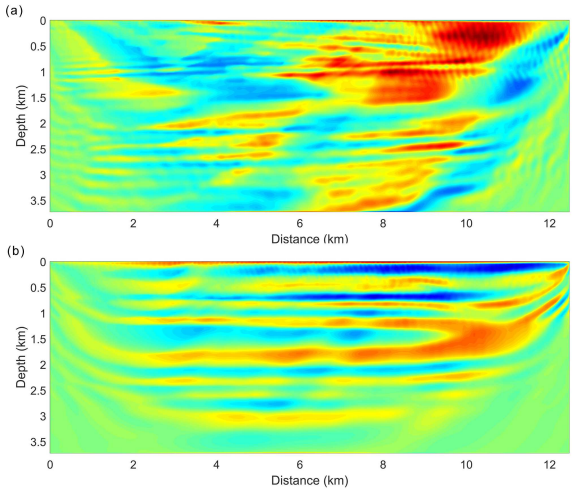

Fig. 15. The raw velocity gradients from (a) GCN, and (b) WECI ($q = 1.5$) using filtered data between 2 Hz and 8 Hz.

longer wavelength updates, and it is more laterally continuous.

After 200 iterations, the resulting inverted velocity model is shown in Figure 16a. Although GCN captures some layered structure of the model, it produces unreasonable updates in the tilted elliptical circle, which may be caused by cycle skipping. The WECI-inverted velocity model is shown in Figure 16b. It shows that WECI captures high-velocity layers in the shallow area (1.5 km-2.0 km depth) and low-velocity layers below them (2.0 km-2.5 km depth).

In the second stage, we refine the resolution of the inverted velocity model. Thus, we filter the real data with a wider frequency range (2 Hz-12 Hz) to include more high frequencies. We still use 200 iterations of optimization in this inversion stage. A subsequent GCN is performed based on the velocity model in Figure 16a, and the result is shown in Figure 17a. It is obvious that more thin layers are captured using the data with a wider frequency range. However, wrong velocity updates also become more severe, as indicated by the tilted elliptical circle. By comparison, a subsequent WECI greatly improves the resolution of the inverted velocity in the second inversion stage, and the layered structures show lateral consistency, as

© 2023 IEEE. Personal use is permitted, but republication/redistribution requires IEEE permission. See https://www.ieee.org/publications/rights/index.html for more information.

This article has been accepted for publication in IEEE Transactions on Geoscience and Remote Sensing. This is the author's version which has not been fully edited and content may change prior to final publication. Citation information: DOI 10.1109/TGRS.2023.3300127

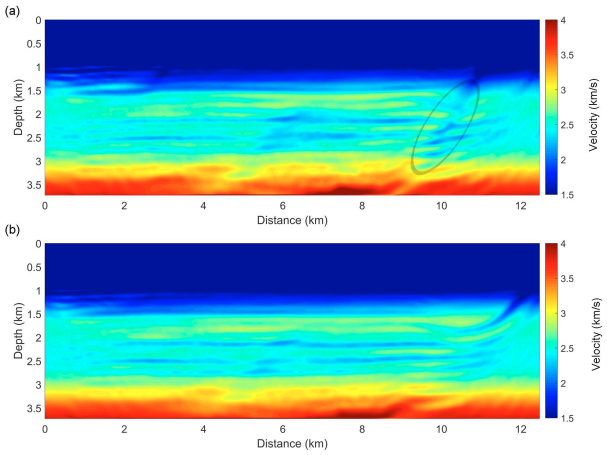

Fig. 16. The inverted velocity models from (a) GCN, and (b) WECI ($q = 1.5$) using filtered data between 2 Hz and 8 Hz.

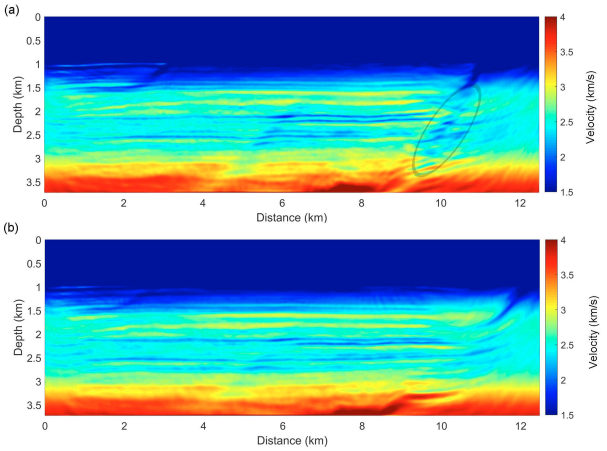

Fig. 17. The inverted velocity models from (a) GCN, and (b) WECI ($q = 1.5$) using filtered data between 2 Hz and 12 Hz.

shown in Figure 17b.

We perform LSRTM using the initial, GCN-inverted, and WECI-inverted velocity models and show the resulting images in Figure 18. We observe that the energy of some events in the LSRTM image from the initial velocity model (Figure 18a) are not well focused compared to the image from the WECI-inverted velocity model (Figure 18c), as indicated by the red arrows. Additionally, some events in the LSRTM image from the GCN-inverted velocity model (Figure 18b) are severely distorted due to the errors in the inverted velocity.

To further verify the accuracy of the proposed WECI method, we compare the inverted velocity models with a well-log velocity profile from the check-shot measurement at a distance of 10.5 km. As shown in Figure 19, the black curve represents the well-log velocity, the green curve represents GCN-inverted velocity, and the red curve represents the WECI-inverted velocity. In multiple areas pointed out by the black arrows, the WECI-inverted velocity fits the well-log velocity profile reasonably well, which indicates the accuracy of WECI in this real data application. By comparison, the GCN-inverted velocity does not agree with the well-log velocity profile, perhaps because it has been affected by cycle

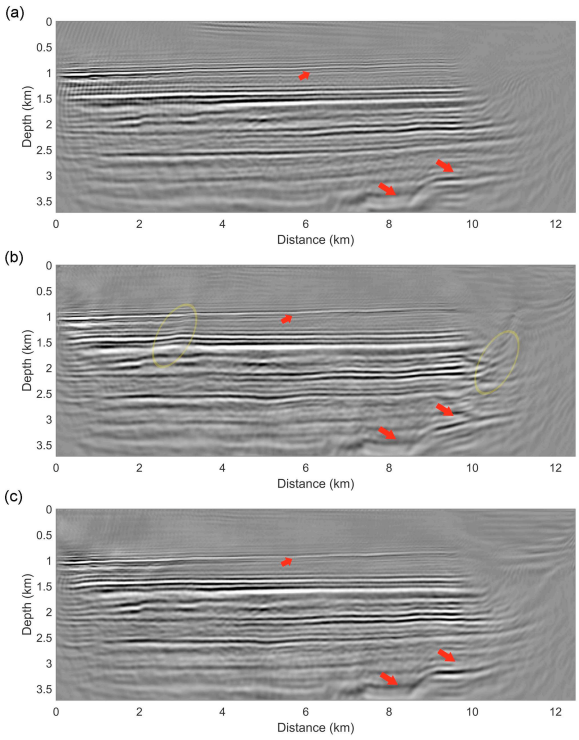

Fig. 18. The LSRTM images from (a) the initial velocity model, (b) GCN-inverted velocity model, and (c) WECI-inverted velocity model ($q = 1.5$).

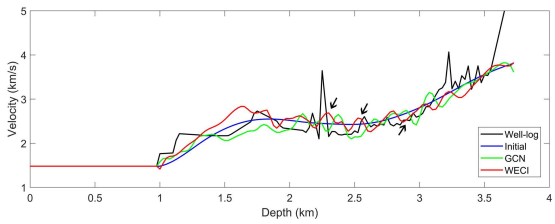

Fig. 19. The vertical velocity profile at 10.5 km (black curve: well-log velocity, blue curve: initial velocity, green curve: GCN-inverted velocity, red curve: WECI-inverted velocity).

skipping. The velocity from WECI is also considered better as it is higher than the well velocity. This is caused by the presence of anisotropy, which has been supported by previous publications [59], [60], [61].

IV. Discussion

The gradient is an important concept across the science and engineering fields. An optimization problem (like seismic waveform inversion) requires the calculation of the gradient to minimize the objective function. The adjoint-state method is a classic method to derive the gradients of the objective functions for waveform inversion methods. As we have shown above, the gradients of different forms of waveform inversions vary. For sophisticated objective functions, the expressions of corresponding gradients are a lot more complicated than that of classic FWI. Their derivations and calculations require significant effort and a rich mathematical background. This acts as an impediment to the development of novel objective functions. Moreover, it is difficult to merge the advantages

© 2023 IEEE. Personal use is permitted, but republication/redistribution requires IEEE permission. See https://www.ieee.org/publications/rights/index.html for more information.

This article has been accepted for publication in IEEE Transactions on Geoscience and Remote Sensing. This is the author's version which has not been fully edited and content may change prior to final publication. Citation information: DOI 10.1109/TGRS.2023.3300127

of different waveform inversions into one single objective function. AD-based waveform inversion can overcome these challenges using the automatic gradient calculation scheme. For the same objective function, AD-based waveform inversion is equally as accurate as conventional waveform inversion using the adjoint-state method [49]. However, AD-based waveform inversion is more efficient to implement, facilitating the development of new forms of FWI. In this paper, we show that AD-based waveform inversion is versatile and effective for different objective functions without an explicit derivation and calculation of the gradient.

In the proposed WECI, we combine the features of ECI and GCN and use the sigmoid function as the weight factor to balance them. We used correlation-based waveform inversions to form the new objective function as we seek to remove the amplitude contribution and make inversion suitable for real data applications. The weight factor defined by the sigmoid function can be dynamically adjusted with the evolution of the optimization. We always use a large weight on the ECI term at the beginning of the inversion. We use ECI to avoid the cycle-skipping issue and build a good background velocity model. Then, the GCN term gradually dominates the inversion and produces high-resolution inversion updates. The weight of WECI can be flexibly controlled according to the quality of the initial velocity model. If the given initial velocity is generally good, larger weights should be imposed on the GCN term. On the contrary, if the quality of the given initial velocity is poor, we should use larger weights on the ECI term to recover the background velocity model.

We find that the power value q of the envelope affects the range of the low-frequency data and the illumination depth of the seismic wave. When q equals 1, we obtain the original data envelope. In this case, the energy of the deep reflections in the data will not be dramatically weakened, and the recovery of the deep structures is possible. However, if the initial velocity model is very far from the true one, we may get wrong velocity updates in the deep area using envelope-based waveform inversions. When q equals 2, the range of the produced low frequencies becomes wider. However, the energy of the deep reflections will be relatively weaker and only the shallow part of the model can be retrieved. To compensate for the limitations of $q = 1$ and $q = 2$, we set $q = 1.5$ for all the examples in this paper. In theory, a dynamic q value (like the weight in WECI) can be used in the optimization process. We can start with a relatively large q value to recover the shallow part. Then, we gradually decrease the q value to estimate the deep structures like the layer-stripping strategy [62], [63]. We will explore this feature in our future research.

V. Conclusions

We demonstrated the versatility and effectiveness of an automatic differentiation (AD)-based waveform inversion for different objective functions. Under the framework of AD-based waveform inversion, we proposed a weighted envelope-correlation inversion (WECI) by combining two correlation-based objective functions, global correlation norm (GCN) and envelope correlation inversion (ECI). These two terms are weighted by a sigmoid function, and the weights can be dynamically adjusted during the optimization process. A large weight is imposed on the ECI in the early stages of the inversion to reconstruct a good background velocity model. Then, in the later stages, the weight imposed on the GCN term gradually increases, and high-wavenumber component updates are provided to refine the resolution of the inverted velocity model. We verified the applicability and accuracy of the proposed WECI method on synthetic and real data.

Acknowledgement

We thank Jilin University for its support and the CLEG group for the collaborative environment. This work was supported by Natural Science Foundation of Jilin Province (20230101082JC), and the special fund of the Key Laboratory of Geophysical Exploration Equipment. We thank CGG for providing the field data set and Geoscience Australia for providing the well-log information.

References

[1] A. Tarantola, "Inversion of seismic reflection data in the acoustic approximation," Geophysics, vol. 49, no. 8, pp. 1259–1266, 1984.
[2] J. Virieux and S. Operto, "An overview of full-waveform inversion in exploration geophysics," Geophysics, vol. 74, no. 6, pp. WCC1–WCC26, 2009.
[3] Y. Wang, Seismic inversion: Theory and applications. John Wiley & Sons, 2016.
[4] R. P. Bording, A. Gersztenkorn, L. R. Lines, J. A. Scales, and S. Treitel, "Applications of seismic travel-time tomography," Geophysical Journal International, vol. 90, no. 2, pp. 285–303, 1987.
[5] B. Lehmann, Seismic traveltime tomography for engineering and exploration applications. Earthdoc, 2007.
[6] Y. Luo and G. T. Schuster, "Wave-equation traveltime inversion," Geophysics, vol. 56, no. 5, pp. 645–653, 1991.
[7] G. Wang, S. Wang, J. Song, C. Dong, and M. Zhang, "Elastic reflection traveltime inversion with decoupled wave equation," Geophysics, vol. 83, no. 5, pp. R463–R474, 2018.
[8] B. Biondi and W. W. Symes, "Angle-domain common-image gathers for migration velocity analysis by wavefield-continuation imaging," Geophysics, vol. 69, no. 5, pp. 1283–1298, 2004.
[9] P. Sava and B. Biondi, "Wave-equation migration velocity analysis. i. theory," Geophysical Prospecting, vol. 52, no. 6, pp. 593–606, 2004.
[10] A. Alali, B. Sun, and T. Alkhalifah, "The effectiveness of a pseudo-inverse extended born operator to handle lateral heterogeneity for imaging and velocity analysis applications," Geophysical Prospecting, vol. 68, no. 4, pp. 1154–1166, 2020.
[11] S. Xu, D. Wang, F. Chen, Y. Zhang, and G. Lambare, "Full waveform inversion for reflected seismic data," in 74th EAGE Conference and Exhibition incorporating EUROPEC 2012. European Association of Geoscientists & Engineers, 2012, pp. cp–293.
[12] G. Yao, D. Wu, and S.-X. Wang, "A review on reflection-waveform inversion," Petroleum Science, vol. 17, no. 2, pp. 334–351, 2020.
[13] B. Chi, L. Dong, and Y. Liu, "Full waveform inversion method using envelope objective function without low frequency data," Journal of Applied Geophysics, vol. 109, pp. 36–46, 2014.
[14] R.-S. Wu, J. Luo, and B. Wu, "Seismic envelope inversion and modulation signal model," Geophysics, vol. 79, no. 3, pp. WA13–WA24, 2014.
[15] Y. Hu, R.-S. Wu, L.-G. Han, and P. Zhang, "Joint multiscale direct envelope inversion of phase and amplitude in the time–frequency domain," IEEE Transactions on Geoscience and Remote Sensing, vol. 57, no. 7, pp. 5108–5120, 2019.
[16] P. Zhang, R.-S. Wu, L.-G. Han, and Y. Hu, "Elastic direct envelope inversion based on wave mode decomposition for multi-parameter reconstruction of strong-scattering media," Petroleum Science, vol. 19, no. 5, pp. 2046–2063, 2022.
[17] T. Van Leeuwen and F. J. Herrmann, "Mitigating local minima in full-waveform inversion by expanding the search space," Geophysical Journal International, vol. 195, no. 1, pp. 661–667, 2013.

© 2023 IEEE. Personal use is permitted, but republication/redistribution requires IEEE permission. See https://www.ieee.org/publications/rights/index.html for more information.

This article has been accepted for publication in IEEE Transactions on Geoscience and Remote Sensing. This is the author's version which has not been fully edited and content may change prior to final publication. Citation information: DOI 10.1109/TGRS.2023.3300127

[18] T. van Leeuwen and F. J. Herrmann, "A penalty method for pde-constrained optimization in inverse problems," Inverse Problems, vol. 32, no. 1, p. 015007, 2015.

[19] C. Song and T. A. Alkhalifah, "Efficient wavefield inversion with outer iterations and total variation constraint," IEEE Transactions on Geoscience and Remote Sensing, vol. 58, no. 8, pp. 5836–5846, 2020.

[20] M. Warner and L. Guasch, "Adaptive waveform inversion: Theory," Geophysics, vol. 81, no. 6, pp. R429–R445, 2016.

[21] L. Guasch, M. Warner, and C. Ravaut, "Adaptive waveform inversion: Practice," Geophysics, vol. 84, no. 3, pp. R447–R461, 2019.

[22] B. Engquist, B. D. Froese, and Y. Yang, "Optimal transport for seismic full waveform inversion," arXiv preprint arXiv:1602.01540, 2016.

[23] L. Métivier, R. Brossier, Q. Merigot, É. Oudet, and J. Virieux, "An optimal transport approach for seismic tomography: Application to 3d full waveform inversion," Inverse Problems, vol. 32, no. 11, p. 115008, 2016.

[24] Y. Yang, B. Engquist, J. Sun, and B. F. Hamfeldt, "Application of optimal transport and the quadratic wasserstein metric to full-waveform inversion," Geophysics, vol. 83, no. 1, pp. R43–R62, 2018.

[25] C. Shin and D.-J. Min, "Waveform inversion using a logarithmic wavefield," Geophysics, vol. 71, no. 3, pp. R31–R42, 2006.

[26] E. Bozdağ, J. Trampert, and J. Tromp, "Misfit functions for full waveform inversion based on instantaneous phase and envelope measurements," Geophysical Journal International, vol. 185, no. 2, pp. 845–870, 2011.

[27] Y. Choi and T. Alkhalifah, "Application of multi-source waveform inversion to marine streamer data using the global correlation norm," Geophysical Prospecting, vol. 60, no. 4-Simultaneous Source Methods for Seismic Data, pp. 748–758, 2012.

[28] J.-W. Oh and T. Alkhalifah, "Full waveform inversion using envelope-based global correlation norm," Geophysical Journal International, vol. 213, no. 2, pp. 815–823, 2018.

[29] A. Richardson, "Generative adversarial networks for model order reduction in seismic full-waveform inversion," arXiv preprint arXiv:1806.00828, 2018.

[30] F. Yang and J. Ma, "Deep-learning inversion: A next-generation seismic velocity model building method," Geophysics, vol. 84, no. 4, pp. R583–R599, 2019.

[31] V. Kazei, O. Ovcharenko, P. Plotnitskii, D. Peter, X. Zhang, and T. Alkhalifah, "Mapping full seismic waveforms to vertical velocity profiles by deep learning," Geophysics, vol. 86, no. 5, pp. R711–R721, 2021.

[32] Z.-d. Zhang and T. Alkhalifah, "High-resolution reservoir characterization using deep learning-aided elastic full-waveform inversion: The north sea field data example," Geophysics, vol. 85, no. 4, pp. WA137–WA146, 2020.

[33] Y. Li, T. Alkhalifah, and Z. Zhang, "Deep-learning assisted regularized elastic full waveform inversion using the velocity distribution information from wells," Geophysical Journal International, vol. 226, no. 2, pp. 1322–1335, 2021.

[34] J. Yao, M. Warner, and Y. Wang, "Regularization of anisotropic full waveform inversion with multiple parameters by adversarial neural networks," Geophysics, vol. 88, no. 1, pp. 1–38, 2022.

[35] O. Ovcharenko, V. Kazei, M. Kalita, D. Peter, and T. Alkhalifah, "Deep learning for low-frequency extrapolation from multioffset seismic data," Geophysics, vol. 84, no. 6, pp. R989–R1001, 2019.

[36] C. Song and Y. Wang, "High-frequency wavefield extrapolation using the fourier neural operator," Journal of Geophysics and Engineering, vol. 19, no. 2, pp. 269–282, 2022.

[37] B. Moseley, A. Markham, and T. Nissen-Meyer, "Solving the wave equation with physics-informed deep learning," arXiv preprint arXiv:2006.11894, 2020.

[38] J. D. Smith, K. Azizzadenesheli, and Z. E. Ross, "Eikonet: Solving the eikonal equation with deep neural networks," IEEE Transactions on Geoscience and Remote Sensing, vol. 59, no. 12, pp. 10 685–10 696, 2020.

[39] T. Alkhalifah, C. Song, U. bin Waheed, and Q. Hao, "Wavefield solutions from machine learned functions constrained by the helmholtz equation," Artificial Intelligence in Geosciences, vol. 2, pp. 11–19, 2021.

[40] U. bin Waheed, E. Haghighat, T. Alkhalifah, C. Song, and Q. Hao, "Pinneik: Eikonal solution using physics-informed neural networks," Computers & Geosciences, vol. 155, p. 104833, 2021.

[41] C. Song, T. Alkhalifah, and U. B. Waheed, "Solving the frequency-domain acoustic VTI wave equation using physics-informed neural networks," Geophysical Journal International, vol. 225, no. 2, pp. 846–859, 2021.

[42] C. Song, Y. Liu, P. Zhao, T. Zhao, J. Zou, and C. Liu, "Simulating multi-component elastic seismic wavefield using deep learning," IEEE Geoscience and Remote Sensing Letters, 2023.

[43] M. Rasht-Behesht, C. Huber, K. Shukla, and G. E. Karniadakis, "Physics-informed neural networks (pinns) for wave propagation and full waveform inversions," Journal of Geophysical Research: Solid Earth, vol. 127, no. 5, p. e2021JB023120, 2022.

[44] C. Song and T. A. Alkhalifah, "Wavefield reconstruction inversion via physics-informed neural networks," IEEE Transactions on Geoscience and Remote Sensing, vol. 60, pp. 1–12, 2022.

[45] U. B. Waheed, T. Alkhalifah, E. Haghighat, C. Song, and J. Virieux, "Pinntomo: Seismic tomography using physics-informed neural networks," arXiv preprint arXiv:2104.01588, 2021.

[46] A. G. Baydin, B. A. Pearlmutter, A. A. Radul, and J. M. Siskind, "Automatic differentiation in machine learning: a survey," Journal of Marchine Learning Research, vol. 18, pp. 1–43, 2018.

[47] A. Paszke, S. Gross, S. Chintala, G. Chanan, E. Yang, Z. DeVito, Z. Lin, A. Desmaison, L. Antiga, and A. Lerer, "Automatic differentiation in pytorch," 2017.

[48] M. Abadi, A. Agarwal, P. Barham, E. Brevdo, Z. Chen, C. Citro, G. S. Corrado, A. Davis, J. Dean, M. Devin et al., "Tensorflow: Large-scale machine learning on heterogeneous distributed systems," arXiv preprint arXiv:1603.04467, 2016.

[49] A. Richardson, "Seismic full-waveform inversion using deep learning tools and techniques," arXiv preprint arXiv:1801.07232, 2018.

[50] W. Zhu, K. Xu, E. Darve, and G. C. Beroza, "A general approach to seismic inversion with automatic differentiation," Computers & Geosciences, vol. 151, p. 104751, 2021.

[51] W. Zhu, K. Xu, E. Darve, B. Biondi, and G. C. Beroza, "Integrating deep neural networks with full-waveform inversion: Reparameterization, regularization, and uncertainty quantification," Geophysics, vol. 87, no. 1, pp. R93–R109, 2022.

[52] Z. Wu and T. Alkhalifah, "Efficient scattering-angle enrichment for a nonlinear inversion of the background and perturbations components of a velocity model," Geophysical Journal International, vol. 210, no. 3, pp. 1981–1992, 2017.

[53] S. Laue, "On the equivalence of forward mode automatic differentiation and symbolic differentiation," arXiv preprint arXiv:1904.02990, 2019.

[54] A. Richardson, "Deepwave," Nov. 2022. [Online]. Available: https://doi.org/10.5281/zenodo.7278382

[55] J. Sun, K. Innanen, T. Zhang, and D. Trad, "Implicit seismic full waveform inversion with deep neural representation," Journal of Geophysical Research: Solid Earth, vol. 128, no. 3, p. e2022JB025964, 2023.

[56] F. Aminzadeh, N. Burkhard, L. Nicoletis, F. Rocca, and K. Wyatt, "Seg/eaeg 3-d modeling project: 2nd update," The Leading Edge, vol. 13, no. 9, pp. 949–952, 1994.

[57] R. Versteeg, "The marmousi experience: Velocity model determination on a synthetic complex data set," The Leading Edge, vol. 13, no. 9, pp. 927–936, 1994.

[58] R. Soubaras and R. Dowle, "Variable-depth streamer–a broadband marine solution," first break, vol. 28, no. 12, 2010.

[59] Z. Wu and T. Alkhalifah, "Waveform inversion for acoustic VTI media in frequency domain," in 2016 SEG International Exposition and Annual Meeting. OnePetro, 2016.

[60] R. Djebbi and T. Alkhalifah, "Frequency domain multiparameter acoustic inversion for transversely isotropic media with a vertical axis of symmetry," Geophysics, vol. 84, no. 1, pp. C1–C14, 2019.

[61] C. Song and T. Alkhalifah, "An efficient wavefield inversion for transversely isotropic media with a vertical axis of symmetry," Geophysics, vol. 85, no. 3, pp. R195–R206, 2020.

[62] Y. Wang and Y. Rao, "Reflection seismic waveform tomography," Journal of Geophysical Research: Solid Earth, vol. 114, no. B3, 2009.

[63] A. Bian and W. Yu, "Layer-stripping full waveform inversion with damped seismic reflection data," Journal of Earth Science, vol. 22, no. 2, pp. 241–249, 2011.

© 2023 IEEE. Personal use is permitted, but republication/redistribution requires IEEE permission. See https://www.ieee.org/publications/rights/index.html for more information.